Journal of Engineering Mathematics **29:** 299–327, 1995.

A priori tests of large eddy simulation of the compressible plane mixing layer

BERT VREMAN, BERNARD GEURTS and HANS KUERTEN
Department of Applied Mathematics, University of Twente, P.O. Box 217, 7500 AE Enschede, The Netherlands

Received 11 November 1993; Accepted in revised form 15 July 1994

Abstract. Three important aspects for the assessment of the possibilities of Large Eddy Simulation (LES) of compressible flow are investigated. In particular the magnitude of all subgrid-terms, the role of the discretization errors and the correlation of the turbulent stress tensor with several subgrid-models are studied. The basis of the investigation is a Direct Numerical Simulation (DNS) of the two- and three-dimensional compressible mixing layer, using a finite volume method on a sufficiently fine grid. With respect to the first aspect, the exact filtered Navier-Stokes equations are derived and all terms are classified according to their order of magnitude. It is found that the pressure dilatation subgrid-term in the filtered energy equation, which is usually neglected in the modelling-practice, is as large as e.g. the pressure velocity subgrid-term, which in general is modelled. The second aspect yields the result that second- and fourth-order accurate spatial discretization methods give rise to discretization errors which are larger than the corresponding subgrid-terms, if the ratio between the filter width and the grid-spacing is close to one. Even if an exact representation for the subgrid-scale contributions is assumed, LES performed on a (considerably) coarser grid than required for a DNS, is accurate only if this ratio is sufficiently larger than one. Finally the well-known turbulent stress tensor is investigated in more detail. A priori tests of subgrid-models for this tensor yield poor correlations for Smagorinsky's model, which is purely dissipative, while the non-eddy viscosity models considered here correlate considerably better.

1. Introduction

Most turbulent flows contain too many scales for a Direct Numerical Simulation (DNS) of the Navier-Stokes equations. A Large Eddy Simulation (LES) tackles this problem by solving only the large scales, while the effect of the small (subgrid-)scales is modelled (e.g. [1, 2]). Many researchers have attempted to validate LES with the use of DNS at relatively low Reynolds numbers (e.g. [3–10]). In such tests of LES two stages can be distinguished: a priori tests and a posteriori tests [5]. A priori tests of LES are performed by filtering a DNS-database in order to calculate the turbulent stress and to compare this quantity with stresses prescribed by subgrid-models. In contrast, a posteriori tests incorporate actual Large Eddy Simulations whose results are compared with those of the filtered DNS. In this paper we present a priori tests, using DNS of the temporal compressible plane mixing layer. A posteriori tests will be presented in a forthcoming article.

Free shear layers occur in many complex problems of practical importance, e.g. the flow behind an airfoil. From a computational point of view, the plane mixing layer, subject of this paper, is the simplest free shear flow. Direct numerical simulations of the incompressible plane mixing layer have been reported in literature a number of times. A two-dimensional study is performed by e.g. Lesieur *et al.* [12], while investigations of the three-dimensional problem, in which transition to turbulence is found, have been presented [15, 16]. Sandham and Reynolds [17] studied the compressible mixing layer, especially focussing on the structures occurring in the early stages of transition. Here we will present two- and three-dimensional simulations of the compressible plane mixing layer and focus on the turbulent flow regime.

Although we observe many differences between the flows in two and three dimensions, several conclusions drawn for LES are remarkably similar in both settings. In particular the role of the discretization errors in LES and the poor correlation of eddy-viscosity models appear to be qualitatively unaffected by the dimension of the flow.

This paper is organised as follows. First we will give the exact filtered equations for compressible flow in section 2. In section 3 we will present a two-dimensional DNS and verify its accuracy. In section 4 this two-dimensional database is used for a priori tests of LES. Three aspects will be examined: the classification of the (subgrid-)terms in the filtered Navier-Stokes equations with respect to their order of magnitude, the role of the discretization errors and, finally, the correlation between the turbulent stress and several subgrid-models. Section 5 is devoted to the analysis of a three-dimensional simulation. We summarize our conclusions in section 6.

2. Filtering the Navier-Stokes equations

The equations for compressible flow are the well-known Navier-Stokes equations. In this section we will deduce the exact system of filtered Navier-Stokes equations, which contains many more subgrid-terms than the corresponding incompressible system. For this purpose we will introduce a convenient functional notation.

The Navier-Stokes equations, which represent conservation of mass, momentum and energy, read

$$\partial_t \rho = -\partial_j(\rho u_j), \tag{1}$$

$$\partial_t(\rho u_i) = -\partial_j(\rho u_i u_j) - \partial_i p + \partial_j \tau_{ij}, \tag{2}$$

$$\partial_t e = -\partial_j((e+p)u_j) + \partial_j(\tau_{ij} u_i) - \partial_j q_j, \tag{3}$$

where the symbols ∂_t and ∂_j denote the partial differential operators $\partial/\partial t$ and $\partial/\partial x_j$ respectively and the summation convention for repeated indices is used. The independent variables t and x_j represent time and the spatial co-ordinates, respectively.

We introduce a functional notation and write this system of equations in the following way:

$$NS(\rho, \mathbf{u}, p, e, \boldsymbol{\tau}, \mathbf{q}) = 0. \tag{4}$$

The velocity vector is denoted by $\mathbf{u}$, while ρ is the density and p the pressure. Moreover, e is the total energy density

$$e = E(\rho, \mathbf{u}, p) = \frac{p}{\gamma - 1} + \frac{1}{2}\rho u_i u_i. \tag{5}$$

The viscous stress tensor $\boldsymbol{\tau}$ is based on the temperature T and velocity $\mathbf{u}$,

$$\tau_{ij} = F_{ij}(\mathbf{u}, T) = \frac{\mu(T)}{Re}\left(\partial_j u_i + \partial_i u_j - \frac{2}{3}\delta_{ij}\partial_k u_k\right), \tag{6}$$

where δ_{ij} is the Kronecker delta and $\mu(T)$ the dynamic viscosity, expressed by Sutherland's law for air,

$$\mu(T) = T^{\frac{3}{2}}\frac{1+C}{T+C} \tag{7}$$

with $C = 0.4$. In addition $\mathbf{q}$ represents the heat flux vector, given by

$$q_j = Q_j(T) = -\frac{\mu(T)}{(\gamma - 1)\,\mathrm{RePr}\,M_R^2}\partial_j T. \tag{8}$$

The temperature T is related to the density and the pressure by the ideal gas law

$$T = G(\rho, p) = \gamma M_R^2 \frac{p}{\rho}. \tag{9}$$

These equations have been made dimensionless by introducing a reference length L_R, velocity u_R, density ρ_R, temperature T_R and viscosity μ_R. In addition, γ, the ratio of the specific heats C_P and C_V, and the Prandtl number Pr are given the values $\gamma = 1.4$ and $\mathrm{Pr} = 0.72$ [18]. The values of the Reynolds number $Re = \rho_R u_R L_R/\mu_R$ and the reference Mach number $M_R = u_R/\sqrt{\gamma R_g T_R}$, where R_g is the universal gas constant, are given for each case separately. Having introduced these notations, the system of equations can be written in a concise form:

$$\begin{aligned} NS(\rho, \mathbf{u}, p, e, \boldsymbol{\tau}, \mathbf{q}) &= 0, \\ e &= E(\rho, \mathbf{u}, p), \\ \tau_{ij} &= F_{ij}(\mathbf{u}, T), \\ q_j &= Q_j(T), \\ T &= G(\rho, p). \end{aligned} \tag{10}$$

In many turbulent flows the ratio between the largest and smallest scales is much too large for these equations to be solved directly and, hence, the equations are filtered. A filter operation extracts the large-scale part $\bar{f}$ from a variable f. In LES a spatial filter is employed,

$$\bar{f}(\mathbf{x}) = \int_\Omega G_\Delta(\mathbf{x} - \xi) f(\xi)\,\mathrm{d}\xi, \tag{11}$$

where Ω is the flow domain and Δ denotes the 'filter width' associated with the kernel G_Δ. The filtered equations that are derived here, are valid when the 'bar-filter' is any linear operator that commutes with the partial differential operators ∂_t and ∂_j. Applying the filter operation to the nonlinear terms in the Navier-Stokes equations leads to filtered quantities which cannot be directly expressed in terms of the filtered dependent variables. Usually, a decomposition of such terms in a part related to the filtered variables and a so-called 'subgrid-term' is made. To avoid subgrid-terms in the continuity equation, Favre [19] introduced a related linear filter operation for compressible flow,

$$\tilde{f} = \frac{\overline{\rho f}}{\bar{\rho}}, \tag{12}$$

which in general does not commute with the partial differential operators. This 'Favre-filter' will be applied to e.g. the velocity vector.

The derivation of the filtered continuity and momentum equations is straightforward; we simply apply the bar-filter to the original equations (1, 2). Deriving an expression for the filtered energy equation is a more tedious task, which can be performed in several ways. Two possible approaches are presented here, leading to different systems of equations, called system I and II respectively. For the first system the filtered variables $\bar{\rho}, \tilde{\mathbf{u}}$ and $\bar{p}$ are used and a modified energy density $\hat{e}$ is introduced in order to retain the equation of state (5)

Table 1. Expressions for the subgrid-terms.

	System I		System II	
	Symbol	Expression	Symbol	Expression
Momentum equation	$A_{1,i}$	$\partial_j(\bar{\rho}a_{ij})$	$C_{1,i}$	$\partial_j\left(\bar{\rho}a_{ij} - \frac{\gamma-1}{2}\bar{\rho}a_{kk}\delta_{ij}\right)$
	$A_{2,i}$	$\partial_j(\bar{\tau}_{ij} - \hat{\tau}_{ij})$	$C_{2,i}$	$\partial_j(\bar{\tau}_{ij} - \breve{\tau}_{ij})$
Energy equation	B_1	$\frac{1}{\gamma-1}\partial_j(\overline{pu_j} - \bar{p}\tilde{u}_j)$	D_1	$\frac{\gamma}{\gamma-1}\partial_j(\overline{pu_j} - \bar{p}\tilde{u}_j)$
	B_2	$\overline{p\partial_k u_k} - \bar{p}\partial_k\tilde{u}_k$	D_2	$\partial_j\left(\frac{1}{2}\bar{\rho}(\widetilde{u_k u_k}u_j - \widetilde{u_k u_k}\tilde{u}_j)\right)$
	B_3	$\partial_j(\bar{\rho}a_{kj}\tilde{u}_k)$	D_3	$\partial_j\left(\frac{\gamma-1}{2}\bar{\rho}a_{kk}\tilde{u}_j\right)$
	B_4	$\bar{\rho}a_{kj}\partial_j\tilde{u}_k$		
	B_5	$\overline{\tau_{kj}\partial_j u_k} - \bar{\tau}_{kj}\partial_j\tilde{u}_k$		
	B_6	$\partial_j(\bar{\tau}_{ij}\tilde{u}_i - \hat{\tau}_{ij}\tilde{u}_i)$	D_4	$\partial_j(\overline{\tau_{kj}u_k} - \breve{\tau}_{kj}\tilde{u}_k)$
	B_7	$\partial_j(\bar{q}_j - \hat{q}_j)$	D_5	$\partial_j(\bar{q}_j - \breve{q}_j)$

for the filtered variables. The second system employs the variables $\bar{\rho}, \tilde{\mathbf{u}}, \breve{e}$ and involves the introduction of a modified pressure, $\breve{p}$, through the equation of state.

System I is symbolically written as:

$$\begin{aligned} NS(\bar{\rho}, \tilde{\mathbf{u}}, \bar{p}, \hat{e}, \hat{\boldsymbol{\tau}}, \hat{\mathbf{q}}) &= \hat{R}, \\ \hat{e} &= E(\bar{\rho}, \tilde{\mathbf{u}}, \bar{p}), \\ \hat{\tau}_{ij} &= F_{ij}(\tilde{\mathbf{u}}, \tilde{T}), \\ \hat{q}_j &= Q_j(\tilde{T}), \\ \tilde{T} &= G(\bar{\rho}, \bar{p}). \end{aligned} \tag{13}$$

It has the same form as the original unfiltered system with two exceptions: the arguments are filtered variables and the right-hand side $\hat{R}$ in the 'NS-component' does not equal zero anymore. The evolution equation for $\hat{e}$ in equation (13) is obtained when the bar filter is applied to the energy equation (3) and the transport equation for the turbulent kinetic energy is subtracted. The right-hand side $\hat{R}$ contains the subgrid-terms,

$$\hat{R} = \begin{pmatrix} 0 \\ -\mathbf{A_1} + \mathbf{A_2} \\ -B_1 - B_2 - B_3 + B_4 + B_5 + B_6 - B_7 \end{pmatrix} \tag{14}$$

As a consequence of adopting the Favre-filter, the filtered continuity equation does not contain any subgrid-term, so the first component of $\hat{R}$ vanishes. The second component represents the subgrid-terms in the momentum equation and consists of three components itself. The first term $A_{1,i} = \partial_j(\bar{\rho}a_{ij})$ contains the turbulent stress tensor, defined as

$$a_{ij} = \widetilde{u_i u_j} - \tilde{u}_i\tilde{u}_j \tag{15}$$

A second subgrid term, $A_{2,i}$, appears in the momentum equation, which is a result of the nonlinearities in the viscous fluxes. Finally the third component of $\hat{R}$ contains the terms B_1 to B_7, which represent the subgrid-terms in the filtered energy equation. The explicit expressions of all subgrid-terms can be found in Table 1.

Next, we present system II which in contrast to system I does not involve a modified energy $\hat{e}$, but a modified pressure $\breve{p}$ and correspondingly a modified temperature $\breve{T}$. This system symbolically has the form:

$$\begin{aligned} NS(\bar{\rho}, \tilde{\mathbf{u}}, \breve{p}, \bar{e}, \breve{\tau}, \breve{\mathbf{q}}) &= \breve{R}, \\ \bar{e} &= E(\bar{\rho}, \tilde{\mathbf{u}}, \breve{p}), \\ \breve{\tau}_{ij} &= F_{ij}(\tilde{\mathbf{u}}, \breve{T}), \\ \breve{q}_j &= Q_j(\breve{T}), \\ \breve{T} &= G(\bar{\rho}, \breve{p}), \end{aligned} \tag{16}$$

with subgrid-terms

$$\breve{R} = \begin{pmatrix} 0 \\ -\mathbf{C_1} + \mathbf{C_2} \\ -D_1 - D_2 + D_3 + D_4 - D_5 \end{pmatrix}, \tag{17}$$

which can be found in Table 1 as well. The modified pressure $\breve{p}$ is related to the filtered pressure, $\bar{p}$, in system I through

$$\breve{p} = (\gamma - 1)\left(\bar{e} - \frac{1}{2}\bar{\rho}\tilde{u}_k\tilde{u}_k\right) = \bar{p} + \frac{1}{2}(\gamma - 1)\bar{\rho}a_{kk}. \tag{18}$$

Similarly, the expression

$$\breve{T} = \gamma M_R^2 \breve{p}/\bar{\rho} = \tilde{T} + \frac{1}{2}\gamma(\gamma - 1)M_R^2 a_{kk}, \tag{19}$$

relates the modified temperature $\breve{T}$ to the filtered temperature $\tilde{T}$. It is not easy to decide which system of equations is to be preferred. Formally both systems are equivalent and can form a suitable starting point for LES-modelling. System II contains fewer subgrid-terms than system I, which is an advantage for modelling. On the other hand, a modified pressure appears in system II. This is a disadvantage, since the pressure is usually an important variable in compressible flows.

In any case, we observe that the filtered equations for compressible flow contain many subgrid-terms. Formally, all these quantities require modelling. In modelling-practice, however, only the subgrid-terms $A_{1,i}$, B_1 and B_3 (for system I), or $C_{1,i}$ and D_1 (for system II) are taken into account. Indeed, it seems reasonable to neglect the subgrid-terms that contain the viscous stress or heat flux, which are relatively small in flows with high Reynolds numbers. However, it does not seem correct to neglect inviscid subgrid-terms, e.g. the pressure dilatation term B_2, which is purely an effect of compressibility. From these considerations it follows that it is necessary to give an indication of the order of magnitude of all subgrid-terms in order to provide a more solid basis for turbulence modelling. To this aim we use the results of direct numerical simulations of the compressible mixing layer, in order to explicitly calculate the magnitude of these terms.

3. DNS of the mixing layer

In this section the two-dimensional temporal compressible mixing layer in a rectangular domain $[0, L_1] \times [-L_2/2, L_2/2]$ is considered. Periodic boundary conditions are imposed

in the x_1-direction, and in the x_2-direction the boundaries are free slip walls. The basic initial velocity profile is the hyperbolic tangent profile $U = \tanh(2x_2/\delta_{\omega,i})$, where $\delta_{\omega,i}$ is the initial value of the vorticity thickness [20]. We obtain the initial temperature profile from the Busemann–Crocco law [21] and the initial pressure distribution is uniform. Since all flow variables are treated as periodic in the x_1-direction, e.g. $\rho(x_1 + nL_1, x_2, t) = \rho(x_1, x_2, t)$, the pressure as obtained from eq. (5) is periodic as well. The reference length L_R is half the initial vorticity thickness, while the reference density, velocity, temperature and dynamic viscosity are the initial upper stream values. A low amplitude perturbation consisting of a sinusoidal wave superimposed on uniform noise and multiplied with a Gaussian in the x_2 direction is initially added to the basic profile. The sinusoidal wave selected corresponds to the most unstable mode according to linear stability theory [22]. L_1 is set equal to twice the wavelength of the most unstable mode, i.e. so-called two-eddy simulations [20] are performed. Alternative perturbations of the mean field have been studied as well. If these perturbations are of sufficiently low amplitude it is known that after a short transient the most unstable mode, as predicted by linear stability theory, becomes dominant automatically. The specific initial perturbation involving noise confined to the near centerline region and a sinusoidal wave, was selected in order to reduce the transient and to save computing time. It is well known that in 2D mixing layers predominantly large scale structures emerge. Hence, this flow forms a first, relatively simple test-case for LES. In 3D the flow develops a turbulent state with many small scale structures, results of which are presented in section 5.

The numerical method is based on a finite volume approach on a uniform grid with central spatial differencing that is second-order accurate in space. The time integration is performed with a second-order accurate explicit four-stage Runge-Kutta method. The spatial discretization employs two distinct control volumes, one for the convective and the other for the viscous terms. For the convective terms, the control volume at a certain vertex is formed by the four cells which meet at the vertex. On the other hand, the center points of these four cells are identified as the corners of the control volume used for the viscous terms. The flux vectors are integrated over the cell faces with the trapezoidal rule [23, 24].

Direct numerical simulations are performed at $M_R = 0.2$ and $M_R = 0.6$ using $Re = 200$. The results of the simulations show that with this numerical method an accurate DNS is obtained. The simulations are qualitatively correct; the fundamental instability grows, saturates and produces two vortices (Fig. 1a), which move towards each other and merge (Fig. 1b) [12]. Since an unforced simulation is considered the total kinetic energy decays due to the molecular dissipation. The subsequent analysis, however, is concerned with the initial roll-up and pairing processes encountered in this flow and the above mentioned decay has no consequences on the results presented here. The DNS is also quantitatively correct, if the resolution is adequate. In the initial, linear regime in which the perturbations of the mean field are small, the growth rate of the most unstable mode as predicted by linear stability theory was recovered with an error well within 0.5% using the grids containing 128^2 and 256^2 cells for both Mach numbers considered (a detailed account can be found in [25]). The accuracy with which the flow field in the DNS is captured is further supported by Fig. 2 ($M_R = 0.2$) and Fig. 3 ($M_R = 0.6$), which present the evolution of the vorticity thickness, obtained from simulations with 64^2, 128^2 and 256^2 cells respectively. The vorticity thickness (the definition is given in [20]) is a relatively sensitive quantity. The results show a clear convergence for both Mach numbers. The time at which the vorticity thickness attains its maximum value corresponds with the pairing of the vortices. A comparison between Figs. 2 and 3 confirms the fact that an increased compressibility slows down the growth of the vorticity thickness in dimensionless time units

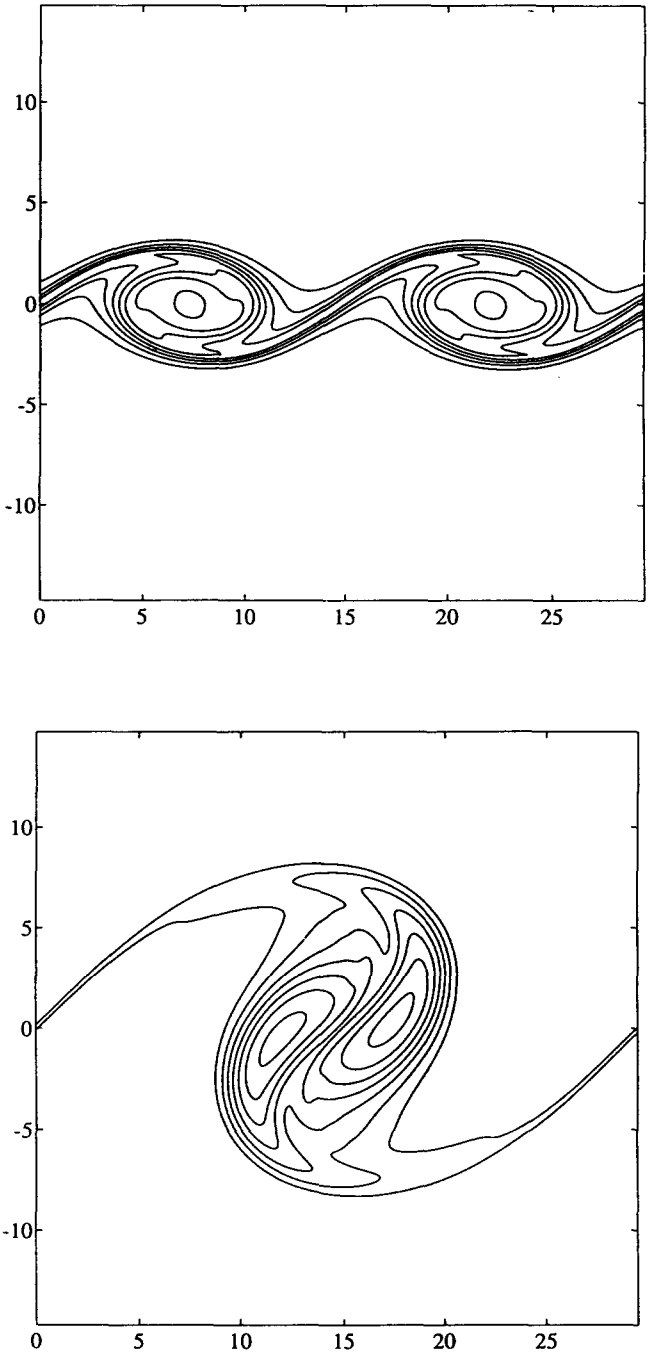

Fig. 1. Contours of spanwise vorticity at $t = 40$ (a) and $t = 100$ (b). The contour increment is 0.1.

[17]. Note, however, that the time unit depends on the Mach number as well. It is a factor three smaller at $M_R = 0.6$ than at $M_R = 0.2$, indicating that in actual time the process is faster at higher Mach numbers. The 256^2-simulation at $M_R = 0.2$ was repeated with a fourth-order accurate finite difference discretization in space for the convective terms. The corresponding

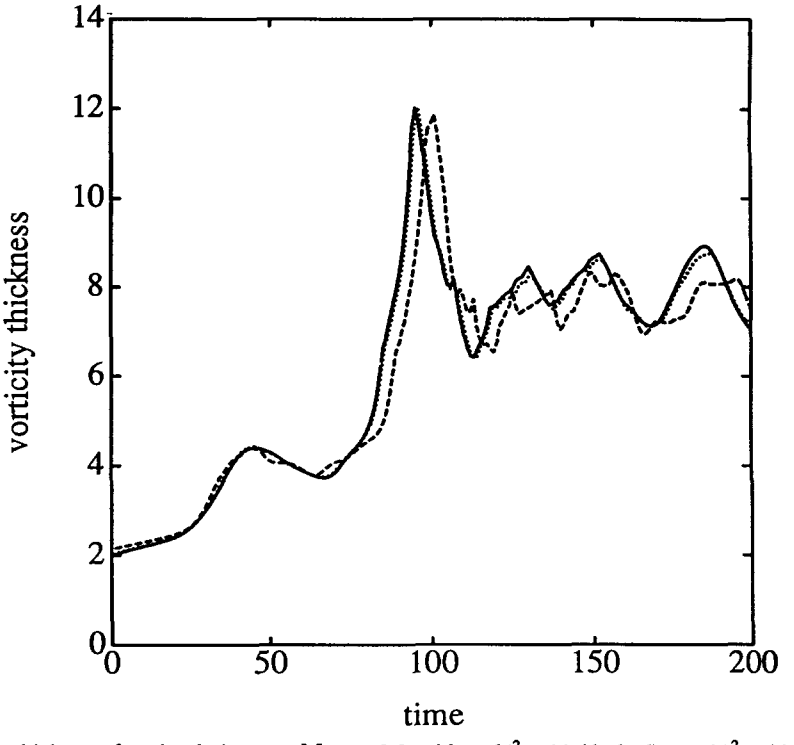

Fig. 2. Vorticity thickness for simulations at $M_R = 0.2$ with a 64^2-grid (dashed), a 128^2-grid (dotted) and a 256^2-grid (solid).

curve of the vorticity thickness coincides with the converged results shown in Fig. 3. We conclude that a DNS with 256^2 cells provides accurate data which can be used to investigate the role of subgrid-terms and discretization errors in LES-studies.

4. Filtering the DNS-data

The numerical procedure to calculate the terms in the filtered Navier-Stokes equations proceeds in a few steps. First the 256^2-DNS-data are filtered with the positive top-hat filter [11], in which the kernel is given by

$$G^{\Delta}(\mathbf{y}) = \begin{cases} \frac{1}{\Delta_1 \Delta_2} & \text{if } |y_i| < \Delta_i/2 \quad (i = 1, 2), \\ 0 & \text{otherwise.} \end{cases} \tag{20}$$

The filter width corresponds with eight cells in each direction ($\Delta_i = L_i/32$), unless stated otherwise. The integration that appears in equation (11) is performed with the trapezoidal rule. As a result, the filter operation yields the filtered quantities occurring in the filtered Navier-Stokes equations defined on the 256^2-grid. Since these quantities are relatively smooth, the spatial derivatives applied to them are accurately calculated with the fourth-order five point central difference on the 256^2-grid (relative error is less than 0.1 percent). Then the terms in the filtered Navier-Stokes equations are restricted to a coarse grid, which contains 64^2 cells of size $h_1 \times h_2$ with $h_i = L_i/64$, so we have $\Delta_i = 2h_i$. This LES-grid is considerably coarser than the DNS-grid, but should be sufficiently fine to perform a well-resolved LES. In 2D the

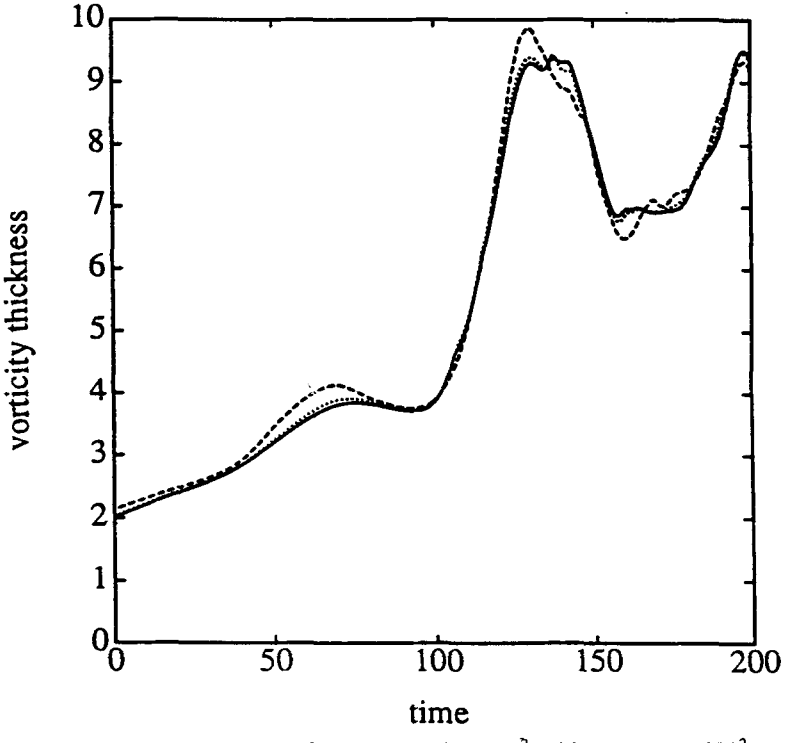

Fig. 3. Vorticity thickness for simulations at $M_R = 0.6$ with a 64^2-grid (dashed), a 128^2-grid (dotted) and a 256^2-grid (solid).

Table 2. Classification of terms in the filtered equations.

	System I		System II	
Category	Mom. equation	Energy equation	Mom. equation	Energy equation
Large	$\partial_j \bar{\rho}\tilde{u}_i\tilde{u}_j + \partial_i \bar{p}$	$\partial_j((\hat{e}+\bar{p})\tilde{u}_j)$	$\partial_j \bar{\rho}\tilde{u}_i\tilde{u}_j + \partial_i \breve{p}$	$\partial_j((\bar{e}+\breve{p})\tilde{u}_j)$
Medium	$\partial_j \hat{\tau}_{ij}$	$\partial_j(\hat{\tau}_{ij}\tilde{u}_j), \partial_j \hat{q}_j$	$\partial_j \breve{\tau}_{ij}$	$\partial_j(\breve{\tau}_{ij}\tilde{u}_j), \partial_j \breve{q}_j$
	$A_{1,i}$	B_1, B_2, B_3	$C_{1,i}$	D_1, D_2
Small		B_4, B_5		D_3, D_4, D_5
Negligible	$A_{2,i}$	B_6, B_7	$C_{2,i}$	

energy spectrum shows a range in which $E \sim k^{-n}$ up to wave numbers $k \approx 25$. For the mixing layer the value of the exponent n is close to 4 as has been observed by others [12] and corresponds with the predictions by Saffman [13]. Alternative, theoretical, predictions suggest different values [14]. The filter-width selected, corresponds to a cut-off at $k \approx 16$, well within this 'inertial range', so that the subgrid terms are quite significant compared to the mean terms, thus constituting a relevant test-case for 2D subgrid term analysis. Finally, the order of magnitude of quantities defined on the LES-grid is measured with the discrete L_2-norm, which is denoted by $\|.\|$.

4.1. CLASSIFICATION OF TERMS

Applying the above procedure to the DNS-data, it appears that all terms in the filtered momentum and energy equations can be grouped into four categories which all have a discrete L_2-norm differing at least one order of magnitude. This ordering of the filtered- and subgrid terms was observed to hold for all stages in the evolution after a well developed roll-up had occurred. We introduce four levels: large (L), medium (M), small (S) and negligible (N). For example, terms a, b, c and d belong to the categories L, M, S and N respectively, if $\|a\| > 10\|b\|, \|b\| > 10\|c\|$ and $\|c\| > 10\|d\|$. Table 2 denotes for each term in the filtered equations to which category it belongs. The table shows that all convective terms are in the category L, while all viscous and heat-flux terms are in the category M. The subgrid-terms appear in the categories M, S and N. From these a priori results we conclude that LES-models should at least focus on the medium subgrid-terms, since they are of the same order of magnitude as the filtered viscous and heat-flux terms, which are always incorporated in a viscous calculation. Moreover, neglecting the terms in classes S and N seems to be allowed from this a priori calculation. Note, however, that it is necessary to verify these conclusions by confronting actual LES results, in which models for the subgrid terms have been introduced, with filtered DNS results [9]. In the following we will discuss the classification in more detail. First we will consider the momentum equations of system I and II, given in equations (13) and (16). Then the energy equations of both systems will be discussed. Finally, we will make some remarks about effects of compressibility.

We turn to the classification of the terms in the momentum equation of system I, found in the second column of Table 2. The sum of the large terms is about 15 times larger than the medium terms, i.e. $\|L\| \approx 15\|M\|$. However, it appears that the two contributions to this sum are approximately 10 times as large as the sum itself, which is expressed by

$$\|\partial_t(\bar{\rho}\tilde{u}_i)\| \approx \|\partial_j(\bar{\rho}\tilde{u}_i\tilde{u}_j) + \partial_i\bar{p}\| \ll \|\partial_j(\bar{\rho}\tilde{u}_i\tilde{u}_j)\| + \|\partial_i\bar{p}\|. \tag{21}$$

This is possibly related to the occurrence of coherent structures, which are vortices in case of the mixing layer. A characterization of a coherent structure is that its lifetime ($\sim \bar{\rho}\tilde{u}_i/\partial_t(\bar{\rho}\tilde{u}_i)$) is much larger than the local turnover time ($\sim \bar{\rho}\tilde{u}_i/\partial_j(\bar{\rho}\tilde{u}_i\tilde{u}_j)$). The norms of the two medium terms in the first component of the momentum equation, the turbulent stress term $\|A_{1,1}\| = \|\partial_j\bar{\rho}a_{1j}\|$ and the viscous flux $\|\partial_j\tilde{\tau}_{1j}\|$ are plotted in Fig. 4. The viscous flux dominates in the initial stage of the simulation, which indicates that the main process in this period is the viscous flattening of the initial profile. Although the turbulent stress is negligible initially, it grows and attains a maximum at the time when the initially prescribed perturbations saturate. So, after a transient stage, the norm of the turbulent stress tensor is comparable to the norm of the filtered viscous term, showing that incorporating the turbulent stress tensor in a subgrid-model is unavoidable. Finally it appears that $\|N\| \approx \|M\|/1000$, which proves that the negligible term is extremely small indeed. All these considerations are nearly the same for the momentum equation of system II (column 4 in Table 2). The most noticeable difference is that the medium subgrid quantity which occurs in this equation, $C_{1,i}$, is about 10% smaller than the turbulent stress $A_{1,i}$. The observation that $\|L\| \approx 15\|M\|$ does not imply that the medium terms are much smaller than the convective terms in all parts of the flow. Indeed, an expression like $\|a\| \ll \|b\|$ means that $|a| \ll |b|$ in most parts of the flow, but regions with $|a| > |b|$ may exceptionally occur. However, in our analysis we have found that only in a relatively small number of isolated grid-points on the LES-grid the medium terms are larger than the convective terms.

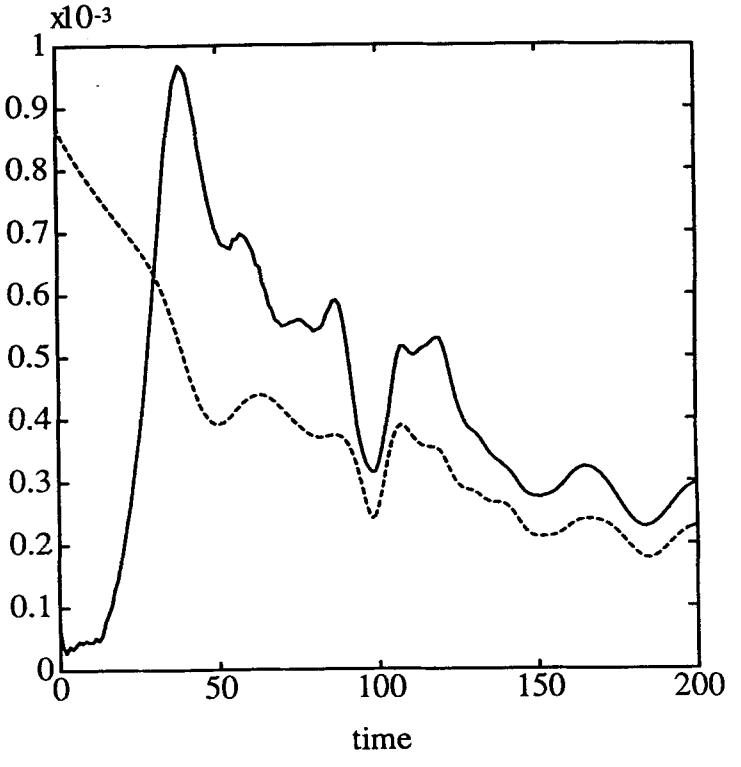

Fig. 4. The subgrid-term $\|\partial_j \bar{\rho} a_{1j}\|$ (solid) and the viscous term $\|\partial_j \hat{\tau}_{1j}\|$ (dashed).

Next we turn to the evolution equation for the energy density of system I (Table 2; column 3). The ratios between the different classes are: $\|L\| \approx 150\|M\|$, $\|M\| \approx 30\|S\|$ and $\|S\| \approx 30\|N\|$. In Fig. 5 the three medium subgrid-terms are shown, which are of the same order of magnitude as the viscous and heat-flux term. It can be observed, that the pressure dilatation subgrid-term B_2 is as large as the other medium subgrid-terms. Therefore, if a subgrid-model is used for this energy equation, also the pressure dilatation subgrid-term appears to require modelling. A posteriori tests should be performed, however, in order to determine which of the subgrid-terms represent the most important contribution in an actual LES. Different terms which, a priori, appear to be of comparable magnitude, can have quite different effects in actual LES [9]. On the other hand, since $\|L\| \approx 150\|M\|$ we expect that the medium subgrid-terms in the energy equation are less essential for LES than the medium subgrid-terms in the momentum equation, where $\|L\| \approx 15\|M\|$. For the energy equation of system II (Table 2; column 5) the ratios between L, M and S are the same as in system I, but negligible terms do not appear. For example the quantity D_5 is an order of magnitude higher than the corresponding quantity B_7 of system I. The difference between D_5 and B_7 is approximately $\partial_j(\mu(\tilde{T})\partial_j a_{kk}/(RePr))$, obtained using relation (19). This contribution is the main consequence of the introduction of a modified temperature, as it appears in system II. This consideration and the fact that the momentum equation of system II contains a modified pressure are the reasons that we prefer system I above system II. Consequently, the remaining part of this study is restricted to the equations of system I.

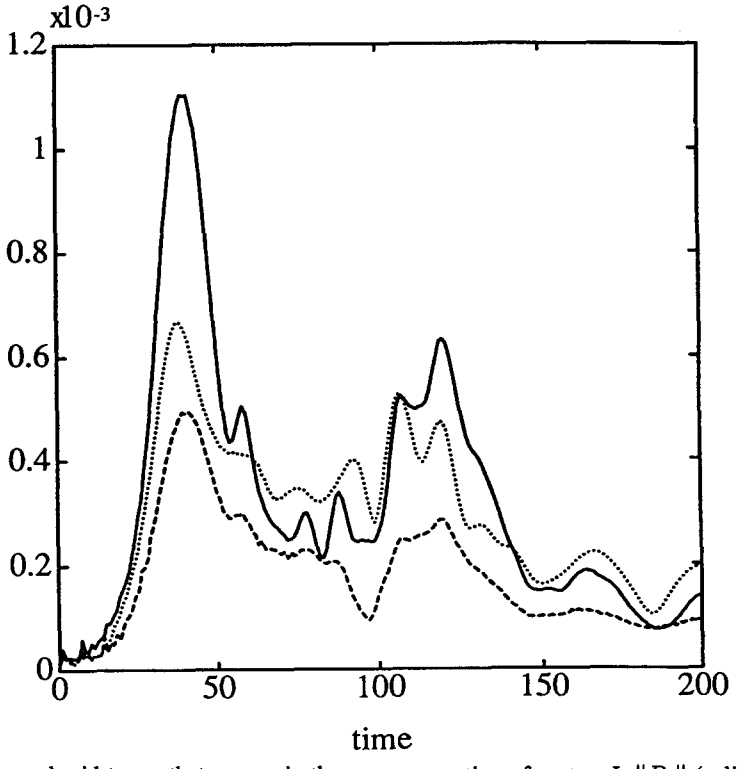

Fig. 5. The medium subgrid-terms that appear in the energy equation of system I: $||B_1||$ (solid), $||B_2||$ (dashed) and $||B_3||$ (dotted).

The discussion so far was restricted to the $M_R = 0.2$ case. We will consider the influence of compressibility next, based on the $M_R = 0.6$ simulation. Firstly, if the Mach number is increased the magnitudes of the non-dimensional convective terms and medium subgrid-terms decrease, while the magnitudes of the viscous and heat-flux terms stay at the same level. This illustrates that the amount of turbulence in the mixing layer decreases, when compressibility is increased. In order to give nonlinear effects a more dominant role in compressible simulations, one could increase the Reynolds number. Secondly, the convective term of the energy equation (e.g. $\partial_j((\hat{e} + \bar{p})\tilde{u}_j)$ of system I) draws our attention. Until the moment of pairing this term is considerably smaller in the $M_R = 0.6$ case than in the $M_R = 0.2$ case, which is obvious when we realise that the pressure is proportional to $1/M_R^2$. However, at the moment of pairing this term strongly increases in the compressible case, which is due to a strong increase of the velocity divergence. Another compressibility effect is the increase of the negligible terms, which become 10 times as large when the Mach number is increased from 0.2 to 0.6. Therefore, although these terms are negligible for the subsonic case, it is not evident that they may be neglected in supersonic and hypersonic simulations.

Finally, it is remarkable that for both $M_R = 0.2$ and $M_R = 0.6$ the pressure dilatation subgrid-term B_2 has relatively the same order of magnitude within the group of medium subgrid-terms in the energy equation of system I. Although this term describes a purely compressible effect, it does not dominate over the other medium subgrid-terms when the Mach number is increased to 0.6. So all medium subgrid-terms in the energy equation equally gain in significance when the Mach number is increased.

4.2. DISCRETIZATION ERRORS

In the sequel a representative subgrid-term and the corresponding discretization error will be compared for three different spatial discretizations and several filter widths. We focus on the non-dissipative part of the filtered momentum-equation in the x_1-direction (as found in system I), which contains a representative convective term, a pressure term and the subgrid term $A_{1,1} = \partial_j(\bar{\rho} a_{1j})$. The subgrid term has been introduced because within a LES the convective term, $\partial_j \overline{\rho u_1 u_j}$, cannot be calculated directly, since it is not expressed in terms of the filtered variables. However, the convective term based on filtered variables, $\partial_j(\bar{\rho}\tilde{u}_1\tilde{u}_j)$, cannot be calculated exactly either, since the quantities $\bar{\rho}$ and $\tilde{u}_j$ are only known at discrete grid points. Similarly, the pressure term introduces a discretization error. Therefore, denoting the discrete spatial derivative operator by δ_j, we obtain

$$\partial_j(\bar{\rho}\tilde{u}_1\tilde{u}_j) + \partial_1\bar{p} = \delta_j(\bar{\rho}\tilde{u}_1\tilde{u}_j) + \delta_1\bar{p} + \beta_1, \tag{22}$$

in which β_1 is the discretization error. So, whereas formally $\partial_j \overline{\rho u_1 u_j} + \partial_1\bar{p}$ is required, only $\delta_j(\bar{\rho}\tilde{u}_1\tilde{u}_j) + \delta_1\bar{p}$ is available in a LES-study. Consequently, there is a total discrepancy $A_{1,1} + \beta_1$, since

$$\partial_j \overline{\rho u_1 u_j} + \partial_1\bar{p} = \delta_j(\bar{\rho}\tilde{u}_1\tilde{u}_j) + \delta_1\bar{p} + A_{1,1} + \beta_1.$$

Whereas the subgrid-term $A_{1,1}$ is usually modelled with a subgrid-model, the discretization error β_1 is not taken into account. The question we address is whether this is justified. We have already described the procedure to calculate subgrid quantities like $A_{1,1}$. The discretization error β_1 is readily calculated as the difference between the fine and coarse grid derivatives, since the operator δ_j in equation (22) is a discretization of the partial derivative on the coarse LES-grid.

Results will be shown for three operators δ_j: the above-mentioned second-order finite volume discretization, the fourth-order five point central difference and a Fourier pseudo-spectral method [16]. As a typical example, the DNS-results for $M_R = 0.2$ at $t = 80$ are used to calculate the magnitudes of $A_{1,1}$ and β_1. At this time the flow is fully developed but not yet oversaturated, since the pairing has not been fully completed. Furthermore, a priori tests at different times have been performed and gave rise to the same conclusions. Figure 6 presents $\|A_{1,1}\|$ and $\|\beta_1\|$ for the second-order, fourth-order and pseudo-spectral method respectively. The variable r is the ratio Δ/h, in which the coarse grid size h is kept constant and corresponds to a grid with 64^2 cells. We observe that $A_{1,1} \sim \Delta^2$ to close approximation and the components of the turbulent stress tensor a_{ij} are of order Δ^2 as well. Next we compare the three discretization methods. If $\Delta = h$, the discretization error β_1 is larger than the subgrid term $A_{1,1}$ for all three methods. Consequently, in this case it is not useful to perform LES even with a perfect subgrid-model. If Δ is sufficiently larger than h, which corresponds to smoother fields on the same 64^2-grid, one finds that $A_{1,1}$ is considerably larger than β_1. In this regime the second-order method shows a small decrease of the discretization error for increasing Δ, whereas the fourth-order finite difference and the pseudo-spectral method show a rapidly decaying discretization error for increasing Δ. Hence, in this regime these two methods are considerably more accurate than the second-order method.

Similar behavior is observed for LES-grids that are coarser or finer than the 64^2-grid. Figure 7 ($\Delta = h$) and Fig. 8 ($\Delta = 2h$) show the norms of subgrid term and discretization errors for several values of the LES-grid size h. In these figures the coarsest and finest grid contain 16^2 and 128^2 cells respectively. We observe that the second-order method is more

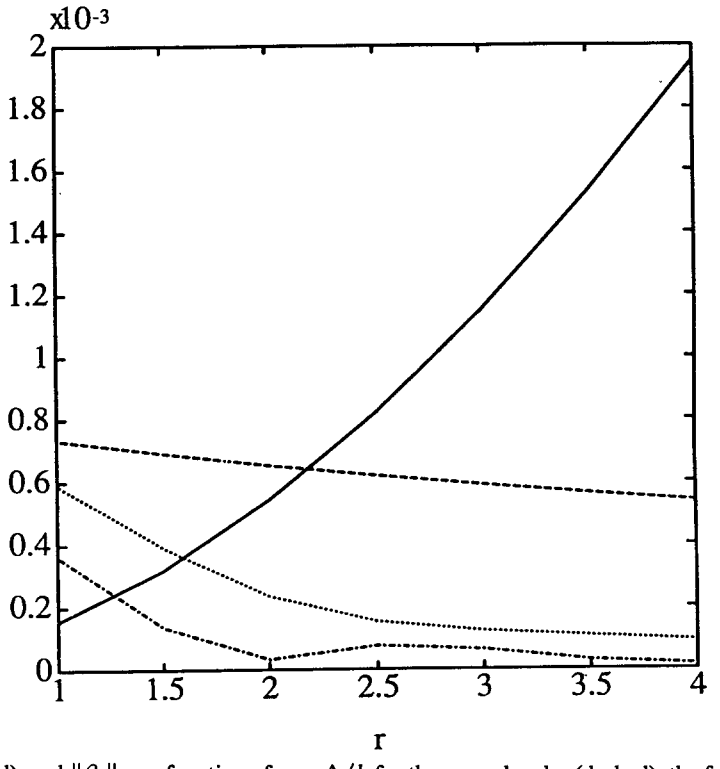

Fig. 6. $\|A_{1,1}\|$ (solid), and $\|\beta_1\|$ as a function of $r = \Delta/h$ for the second-order (dashed), the fourth-order (dotted) and the pseudo-spectral method (dashed-dotted); 64^2-grid.

accurate than the fourth-order method for coarse LES-grids. Moreover, we again notice that all three discretization methods yield discretization errors that are larger than the subgrid term when $\Delta = h$. These observations can serve as a guidance in deciding about appropriate (Δ, h) combinations for a specific spatial discretization method on a given grid. When Δ is increased the filtered fields become smoother which reduces the discretization error as is shown in Figs. 6–8. These smoothed fields, however, also contain progressively less information about the smaller scales. Hence, it is impractical to adopt a very large value of Δ in view of discretization errors alone, but rather select a 'minimal' value of Δ such that the effects of the discretization errors on the simulation remain within reasonable bounds. In view of the above results we expect $\Delta = 2h$ to be a reasonable choice in combination with fourth order or spectral discretization methods. For a second order accurate method a higher value of Δ appears to be required in view of the influence of the discretization error, at the expense of obtaining less information of the smaller scales in the flow [26]. A study of actual LES can further clarify this point.

4.3. SUBGRID MODELLING

The DNS-results provide the possibility to investigate the quality of the subgrid-modelling. In this paper we will only consider the modelling of the subgrid-terms in the momentum-

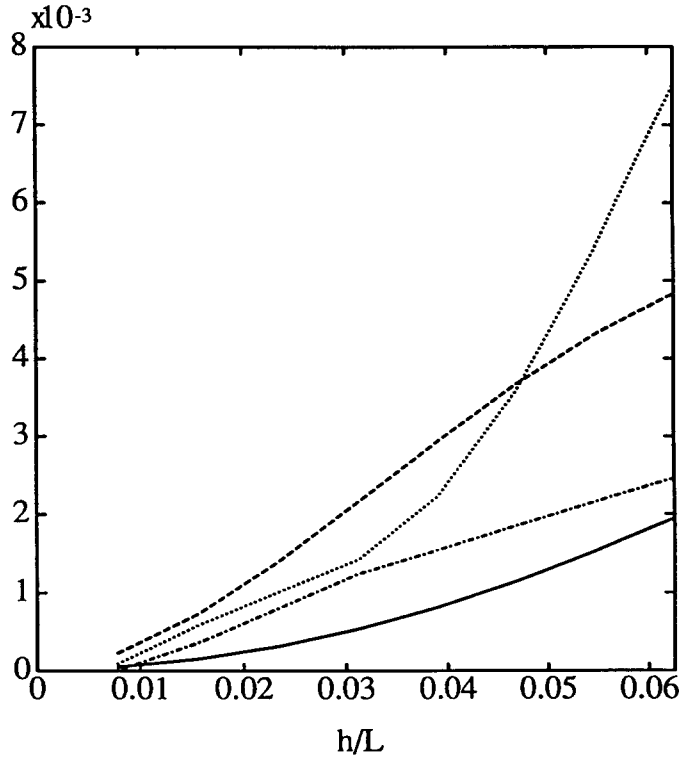

Fig. 7. Subgrid-term $\|A_{1,1}\|$ (solid) and discretization error $\|\beta_1\|$ as a function of h for the second-order (dashed), the fourth-order (dotted) and the pseudo-spectral method (dashed-dotted); $\Delta = h$.

equations. Three models for the turbulent stress tensor a_{ij} will be investigated. The most well-known subgrid model is Smagorinsky's model [1], given by

$$a_{ij}^S = \nu_t S_{ij}, \tag{23}$$

with eddy-viscosity

$$\nu_t = (C_S \Delta)^2 S_{ij} \partial_j \tilde{u}_i, \tag{24}$$

and

$$S_{ij} = \partial_j \tilde{u}_i + \partial_i \tilde{u}_j - \frac{2}{3}\delta_{ij}\partial_k \tilde{u}_k. \tag{25}$$

C_S is the Smagorinsky constant, which we choose equal to 0.17 as suggested in the literature [27]. Smagorinsky's model is an eddy-viscosity model; the following two models are not of this type.

Clark *et al.* [3] have derived a model for the cross-term component of the turbulent stress in incompressible flow, making use of Taylor expansions for the filtered velocity. With the same technique an expansion for the complete turbulent stress a_{ij} is obtained. The lowest order term in Δ in this expansion can be proposed as subgrid-model (noted by Germano [28] as well). When we perform a similar analysis for the Favre-filtered velocities in compressible LES, it

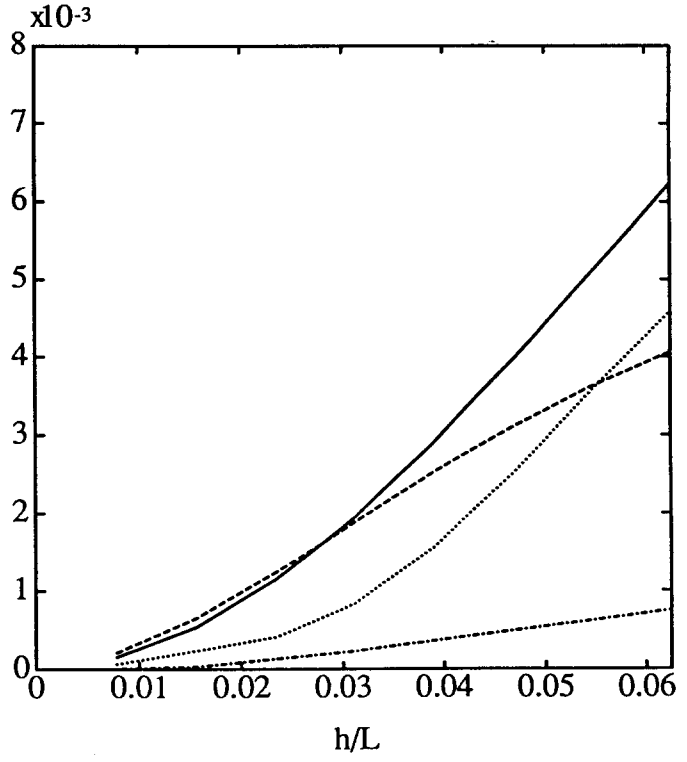

Fig. 8. Subgrid-term $\|A_{1,1}\|$ (solid) and discretization error $\|\beta_1\|$ as a function of h for the second-order (dashed), the fourth-order (dotted) and the pseudo-spectral method (dashed-dotted); $\Delta = 2h$.

appears that the lowest order term in the expansion of a_{ij} is the same as in the incompressible case. Hence, the second subgrid-model which we consider is given by

$$a_{ij}^C = \frac{1}{12}\Delta^2(\partial_k\tilde{u}_i)(\partial_k\tilde{u}_j). \tag{26}$$

The third model which we will discuss is Bardina's scale similarity model [29],

$$a_{ij}^B = \overline{\tilde{u}_i\tilde{u}_j} - \bar{\tilde{u}}_i\bar{\tilde{u}}_j. \tag{27}$$

Here it is assumed that the turbulent stress a_{ij} is described by the resolved turbulent stress a_{ij}^B. The extra filtering in equation (27) is not performed with the Favre-filter, but the 'bar-filter' is applied. The reason is that an explicit calculation of a Favre-filtered quantity (e.g. $\tilde{\tilde{u}}_i$) requires the unfiltered density ρ, which is not available in an actual LES.

We will test the performance of these models by calculating norms and correlations. Comparison of the norm of the modelled turbulent stress with the norm of the exact turbulent stress indicates whether the model correctly predicts the average value of the turbulent stress. Moreover, the correlation of the modelled turbulent stress with the exact turbulent stress measures the quality of the spatial structure of the modelled turbulent stress. The tests are performed on vector level, i.e. we consider the divergences of the turbulent stress tensor, which occur in the momentum equation. In Fig. 9 $\|\partial_j\bar{\rho}a_{1j}\|$ is compared with the corresponding norms of the three subgrid-models, whereas Fig. 10 is a similar plot for the subgrid-term that

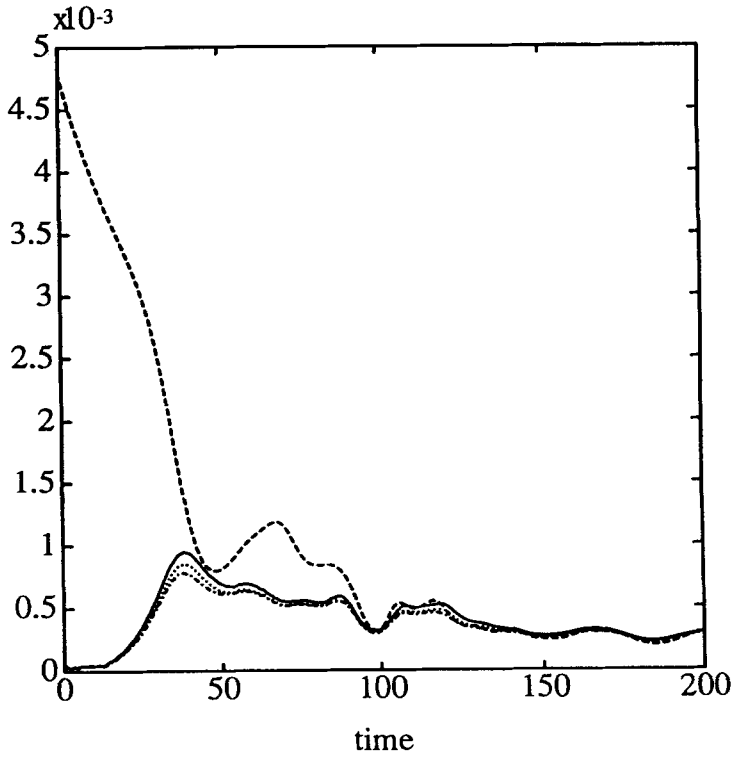

Fig. 9. The subgrid-term $\|\partial_j \bar{\rho} a_{1j}\|$ (solid) and the corresponding models of this term: $\|\partial_j \bar{\rho} a_{1j}^S\|$ (dashed), $\|\partial_j \bar{\rho} a_{1j}^C\|$ (dotted) and $\|\partial_j \bar{\rho} a_{1j}^B\|$ (dashed-dotted).

is found in the momentum equation in the x_2-direction. Moreover, Figs. 11 and 12 show the correlations for the terms $\partial_j \bar{\rho} a_{1j}$ and $\partial_j \bar{\rho} a_{2j}$ respectively.

In Fig. 9 we observe that Smagorinsky's model is much too dissipative in the transitional regime of the simulation (as also observed by Piomelli [5]) but that beyond the moment of pairing the norm of the subgrid-terms is quite reasonably predicted for the value of $C_S = 0.17$. However, the spatial structure of the turbulent stress is not adequately modelled at all, which can be inferred e.g. from the correlation coefficients for Smagorinsky's model which are low and heavily fluctuating in time (Figs. 11 and 12). In principle, this model represent the trace-free part of the turbulent stress only, so we should compare a_{ij}^S with $a_{ij} - (2/3)\delta_{ij} a_{kk}$. However, such a comparison shows that the performance of the model is worse than when it is simply compared with a_{ij} (as above), although the difference is not large.

When we turn to the other two models, we observe that their performance is excellent with respect to both their magnitude and their spatial structure with correlations higher than 0.95. We observe that both models slightly underpredict the turbulent stress. In contrast to eddy-viscosity models, these two models easily lead to instabilities when used in an actual LES for the two-dimensional mixing layer. Numerical instabilities caused by a different subgrid-model are reported in [30, 31]. Such instabilities, which in some cases can be interpreted as a negative eddy-viscosity, should be overcome before an a posteriori test of LES with these subgrid-models is possible. Results of this study will be presented in the future.

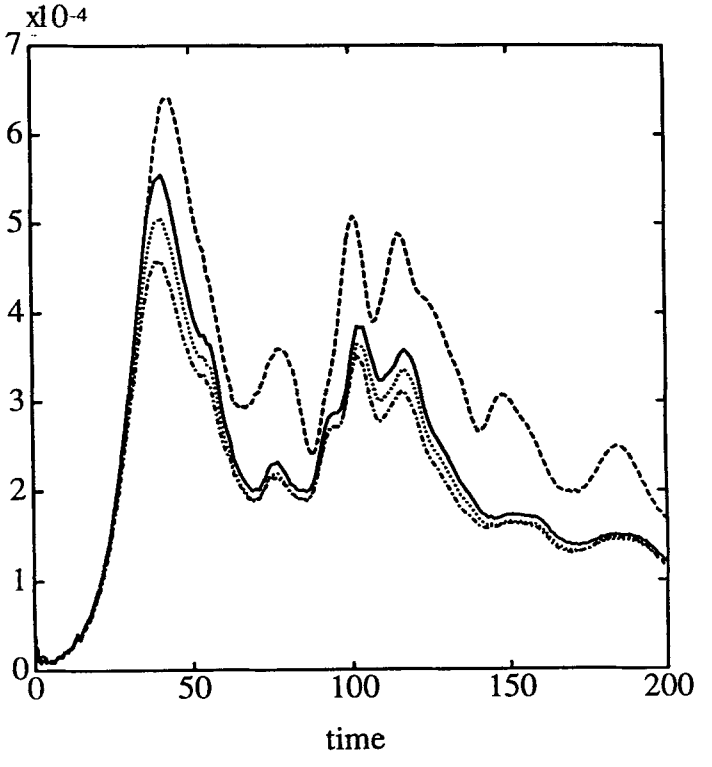

Fig. 10. The subgrid-term $\|\partial_j \bar{\rho} a_{2j}\|$ (solid) and the corresponding models of this term: $\|\partial_j \bar{\rho} a_{2j}^S\|$ (dashed), $\|\partial_j \bar{\rho} a_{2j}^C\|$ (dotted) and $\|\partial_j \bar{\rho} a_{2j}^B\|$ (dashed-dotted).

The excessive dissipation of Smagorinsky's model in the transitional regime is not observed in Fig. 10, but only in Fig. 9, which corresponds to the momentum equation for $\overline{\rho u_1}$. If an eddy-viscosity model is applied, the largest contribution to the subgrid-terms in the transitional stage is given by the term $-\partial_2(\bar{\rho}\nu_t \partial_2 \tilde{u}_1)$. This term, which occurs in $\partial_j \rho a_{1j}^S$, but not in $\partial_j \rho a_{2j}^S$, is initially large, since the initial mean profile is given by $u_1 = \tanh y$. Consequently, the excessive dissipation of an eddy-viscosity model in the transitional stage is due to the presence of mean shear. Beyond the moment of pairing the other components of the rate of strain tensor become important as well and the norm of the subgrid terms corresponding to the dissipation of the remaining vortex is well approximated with the Smagorinsky model.

In the momentum equations the turbulent stress occurs on vector-level, but it is also interesting to consider the turbulent stress on tensor-level, i.e. to consider the components of a_{ij}. Here we will restrict the discussion to a_{12}, the cross component of a_{ij}. Firstly we will discuss a widely used decomposition of a_{12} and then the spatial structure of a_{12} will be analysed.

The turbulent stress can be decomposed into three parts (e.g. [2]),

$$a_{ij} = L_{ij} + C_{ij} + R_{ij}. \tag{28}$$

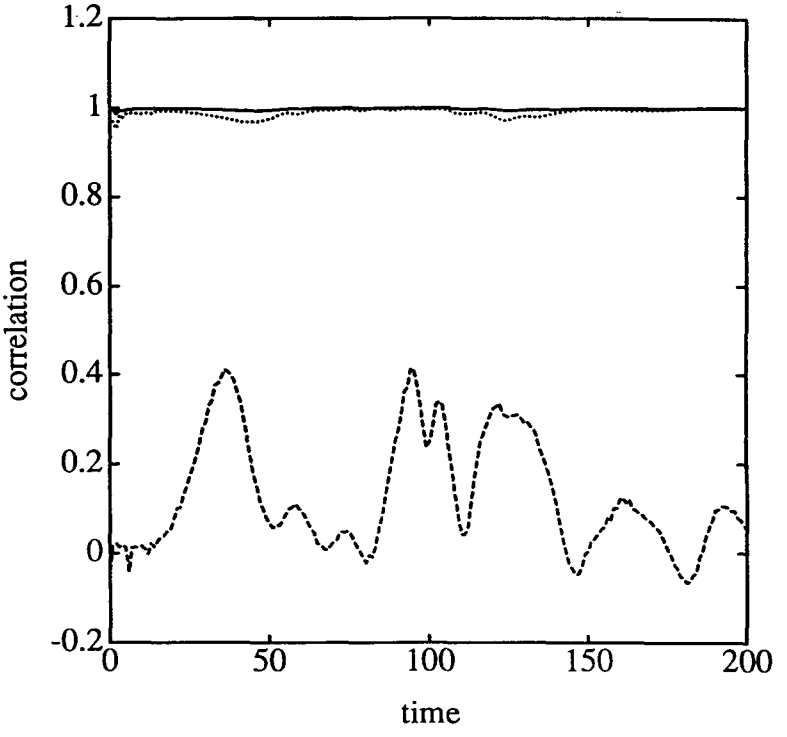

Fig. 11. Correlations of the subgrid term $\|\partial_j \bar{\rho} a_{1j}\|$ with $\|\partial_j \bar{\rho} a_{1j}^S\|$ (dashed), $\|\partial_j \bar{\rho} a_{1j}^C\|$ (solid) and $\|\partial_j \bar{\rho} a_{1j}^B\|$ (dotted).

The tensors L_{ij}, C_{ij} and R_{ij} which are called Leonard-, cross- and Reynolds-stresses respectively, are defined as

$$L_{ij} = \widetilde{\tilde{u}_i \tilde{u}_j} - \tilde{u}_i \tilde{u}_j,$$
$$C_{ij} = \widetilde{\tilde{u}_i u_j''} + \widetilde{u_i'' \tilde{u}_j},$$
$$R_{ij} = \widetilde{u_i'' u_j''},$$

where $u_i'' = u_i - \tilde{u}_i$ denotes the small-scale component of the velocity. In Fig. 13 the norms of a_{12}, L_{12}, C_{12} and R_{12} are plotted. Firstly, we observe that R_{12} has only a very small contribution to a_{12}. This may be due to the fact that in the mixing layer large-scale structures are found, which mainly contribute to the Leonard- and cross-terms when they are filtered. Another reason is that for two-dimensional turbulence the slope of the energy spectrum is steeper than for three-dimensional turbulence. In 3D the role of R_{12} is more important [27], although in that case L_{12} and C_{12} are important as well [3]. The fact that R_{12} is small also explains the poor correlation of Smagorinsky's model, since this model has been developed for flows in which R_{12} is dominant. Moreover, Fig. 13 shows that both L_{12} and C_{12} are larger than in their sum $L_{12} + C_{12}$. Consequently, if one attempts to model these terms one should model them both. It is more justifiable to neglect them both than to take into account only one of them [32].

Next we show the spatial structure of a_{12} in Fig. 14a at $t = 140$, that is after pairing. It is observed that the turbulence intensity is not maximum at the core of the vortex, but away from the core and, moreover, a 'saddle'-structure is apparent. This can be analysed by introducing a

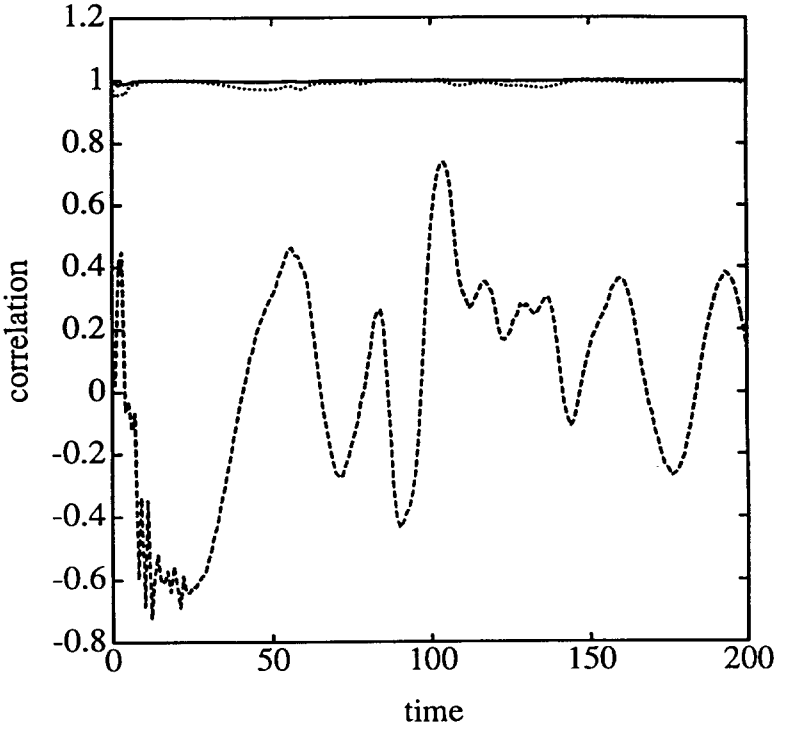

Fig. 12. Correlations of the subgrid term $\|\partial_j \bar{\rho} a_{2j}\|$ with $\|\partial_j \bar{\rho} a_{2j}^S\|$ (dashed), $\|\partial_j \bar{\rho} a_{2j}^C\|$ (solid) and $\|\partial_j \bar{\rho} a_{2j}^B\|$ (dotted).

simple vortex model, as will be shown below. The vortex appears to be approximately radially symmetric with a Gaussian shape, so we introduce polar coordinates (r, θ) and assume

$$\omega(r) = be^{-cr^2} \quad \text{with} \quad b < 0, c > 0, \tag{29}$$

where ω is the vorticity. If we use the additional assumptions $v_\theta = 0$ in the core of the vortex and $v_r = 0$, the velocity component v_θ is obtained by integration of the vorticity,

$$v_\theta(r) = \frac{1}{r}\int_0^r s\omega(s)\,\mathrm{d}s = \frac{-b}{2cr}(e^{-cr^2} - 1). \tag{30}$$

This velocity profile satisfies the stationary incompressible Euler equations in polar coordinates. As a result of these simplifying assumptions, the momentum equation in the radial direction reduces to

$$-\rho v_\theta^2/r = -\partial_r p, \tag{31}$$

which implies $\partial_r p > 0$. It follows that the pressure attains a minimum in the vortex core, which is also observed in our simulations.

Having introduced this vortex model, we derive an expression which gives the spatial structure of a_{12}. If the top-hat filter is used, one can proof that

$$a_{12} = \frac{\Delta^2}{12}\nabla u_1 \cdot \nabla u_2 + O(\Delta^4) \tag{32}$$

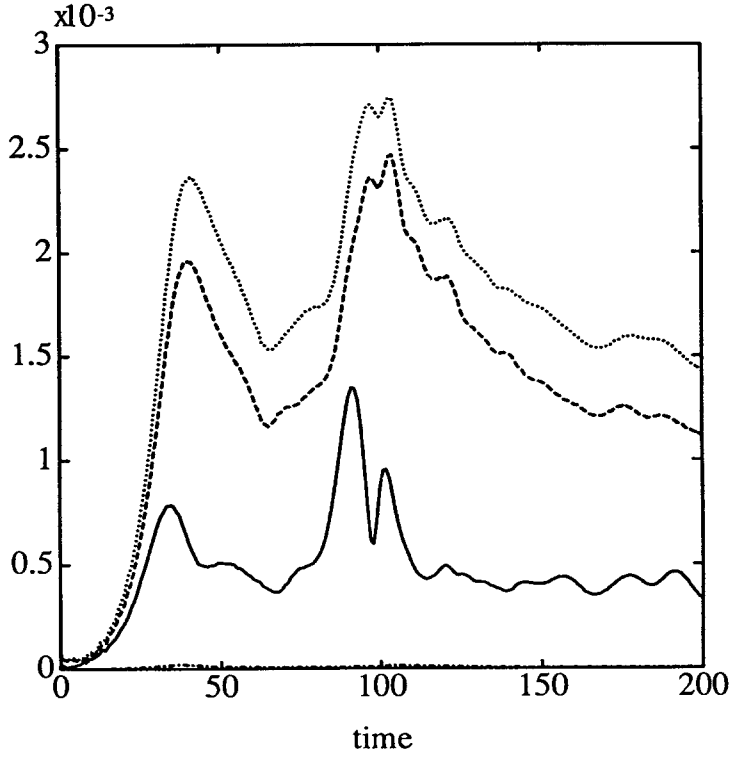

Fig. 13. Decomposition of the turbulent stress $\|a_{12}\|$ (solid): $\|C_{12}\|$ (dashed), $\|L_{12}\|$ (dotted) and $\|R_{12}\|$ (dashed-dotted).

(compare equation (26)). In this case the Cartesian velocity components u_i are

$$u_1 = -v_\theta(r)\sin\theta$$
$$u_2 = v_\theta(r)\cos\theta$$

When we substitute this in equation (32) and use the expression for ∇u_i in polar coordinates, we obtain

$$a_{12} = \frac{\Delta^2}{24}\sin(2\theta)((v_\theta/r)^2 - (\partial_r v_\theta)^2) + O(\Delta^4). \tag{33}$$

Finally equation (30) is substituted in this expression, which yields

$$a_{12} = \frac{\Delta^2 b^2}{24cr^2}\sin(2\theta)e^{-cr^2}\left[1 - \frac{1+cr^2}{e^{cr^2}}\right] + O(\Delta^4), \tag{34}$$

in which the sign of the expression between the square brackets is positive. In Fig. 14b the lowest order term of equation (34) is shown for the values of $b = -0.68$ and $c = 0.04$, which gives a good approximation for the intensity and the radius of the vortex structure. We observe a reasonable agreement with Fig. 14a. A similar analysis can be performed for the diagonal components of a_{ij}, but then the agreement is much less satisfactory, showing that the assumed Gaussian structure of the vortex core constitutes only a rough representation.

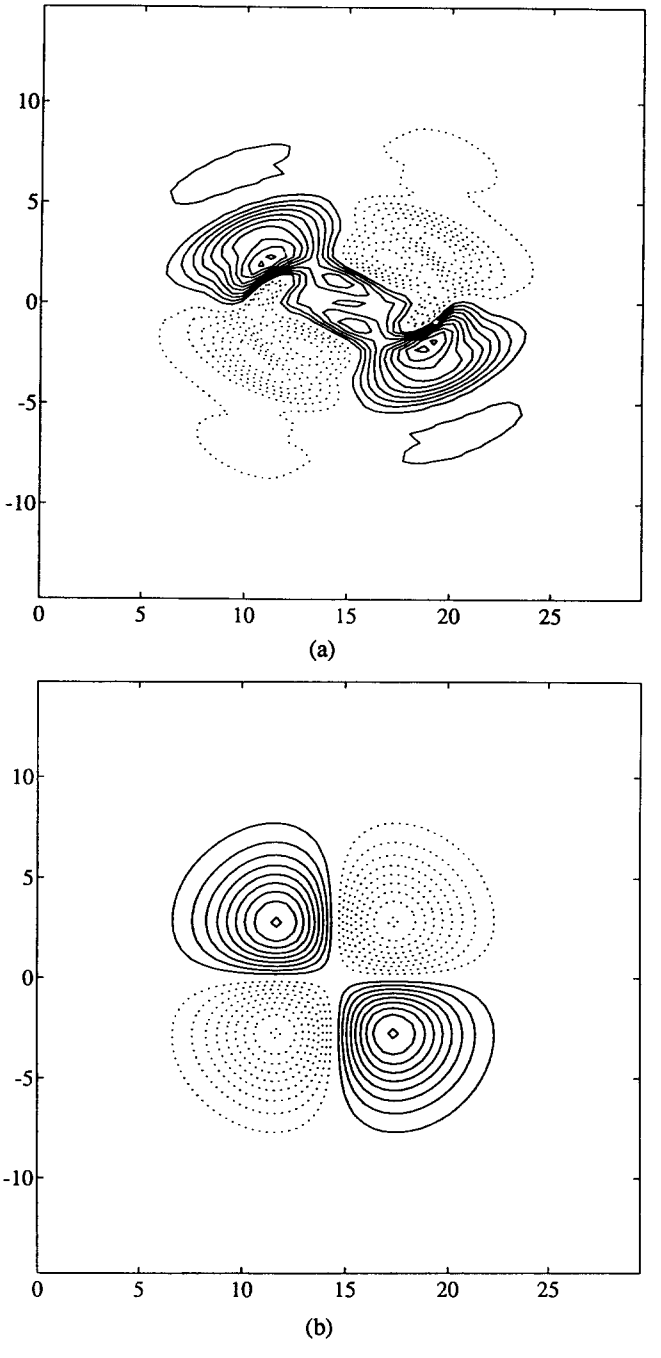

Fig. 14. Contours of the a_{12}-component of (a) the exact turbulent stress and (b) the turbulent stress derived from the vortex model. Solid contours and dotted contours correspond with negative and positive values respectively. The contour increment is 0.0002.

We have discussed the turbulent stress on vector-level, on tensor-level and finally we turn to the turbulent stress on scalar-level, as it occurs in the production term of the equation of turbulent kinetic energy:

$$P = -\bar{\rho} a_{ij} \partial_j \tilde{u}_i. \tag{35}$$

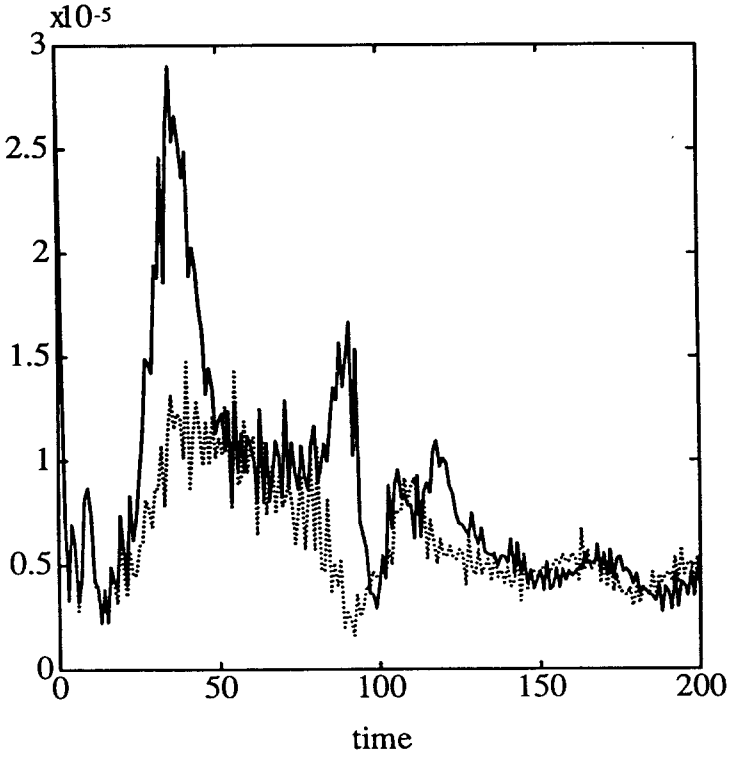

Fig. 15. Decomposition of the production term: $\|P_+\|$ (dotted) and $\|P_-\|$ (solid).

If the eddy-viscosity hypothesis given in equation (23) is valid, P is positive as can easily be proven. Following ref. [6] we split this term into two parts $P = P_+ - P_-$, with

$$P_+ = (|P| + P)/2 \quad \text{and} \quad P_- = (|P| - P)/2 \tag{36}$$

In regions of the flow where P is positive, energy flows from the resolved scales to subgrid scales, whereas if P is negative, the transfer of energy is in the reverse direction. Consequently, P_+ and P_- are interpreted as forward scatter and backscatter respectively. In Fig. 15 the norms P_+ and P_- are plotted as a function of time. It follows that both quantities are of comparable size during a significant part of the simulation, which implies that an eddy-viscosity model, which does not produce any backscatter, is not an accurate subgrid model for the two-dimensional mixing layer. This result is in agreement with the observation that the correlation of the Smagorinsky model with the exact turbulent stress is poor. Backscatter is not restricted to turbulence in two dimensions, but is also important in three-dimensional transitional and turbulent flows [6].

5. The mixing layer in 3D

In sections 3 and 4 we have discussed the DNS and filtering of results of the mixing layer in two dimensions. In this section we present results obtained for the three-dimensional case.

We consider the temporal compressible mixing layer in a cubic geometry. Periodic boundary conditions are imposed in the x_1 – and x_3-direction, while in the x_2 direction the boundaries are free slip walls. As in other simulations of the three-dimensional mixing layer [15, 16], the

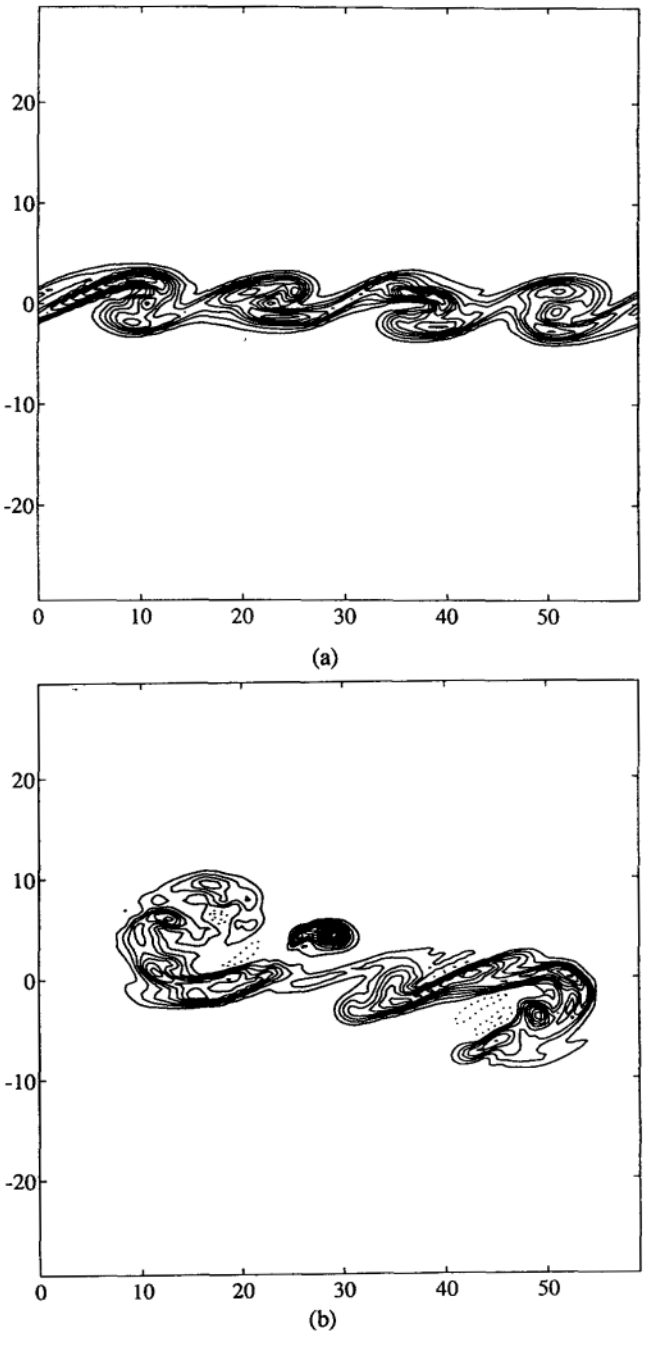

Fig. 16. Contours of spanwise vorticity for the plane $z = 0.75L_3$ at (a) $t = 20$, (b) $t = 40$ and (c) $t = 80$. Solid contours and dotted contours indicate negative and positive vorticity respectively. The contour increment is 0.2.

length L_1 of the domain is set equal to four times the wavelength of the most unstable mode. Superimposed on the mean profile we put a three-dimensional large amplitude perturbation, as described in [17]. In this 3D-case we only consider the case $M_R = 0.2$ and use $Re = 50$ [16].

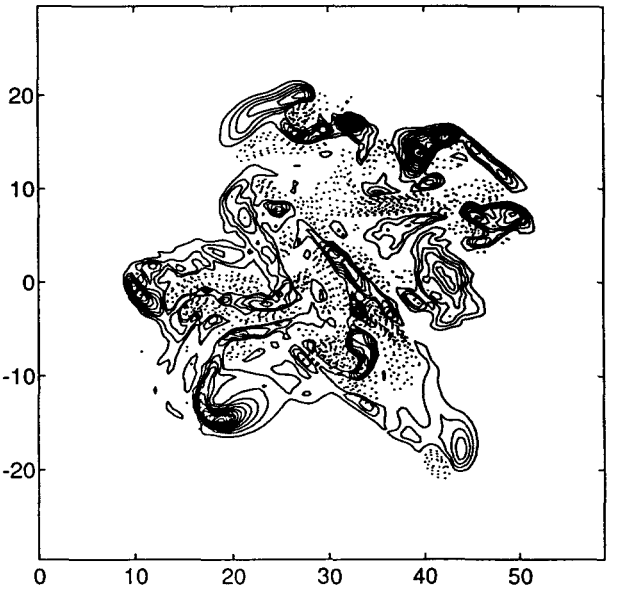

(c)

Fig. 16. (Continued)

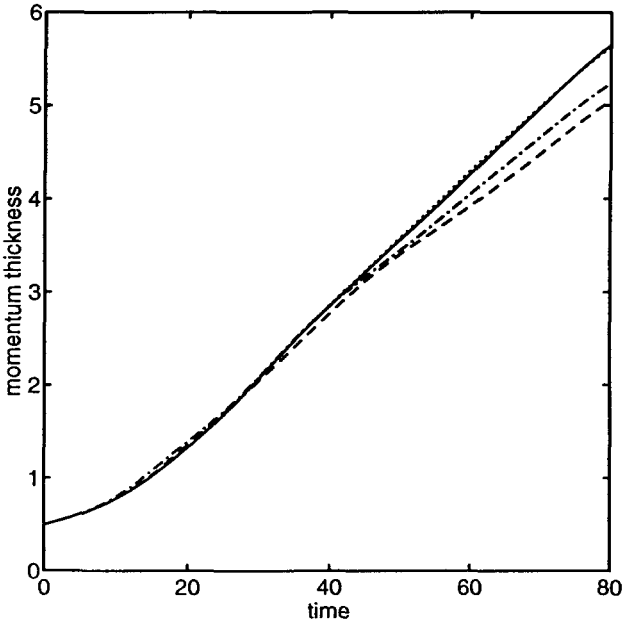

Fig. 17. Momentum thickness for simulations at several grids with several numerical methods: 64^3-grid and second-order (dashed), 64^3-grid and fourth-order (dashed-dotted), 128^3-grid and second-order (solid), 128^3-grid and fourth-order (dashed).

A direct numerical simulation is performed with the second-order accurate finite volume method described in section 3 on a grid with 128^3 cells. The scenario of the simulation consists of a roll-up and successive pairings of the spanwise vorticity (Fig. 16). At $t = 20$

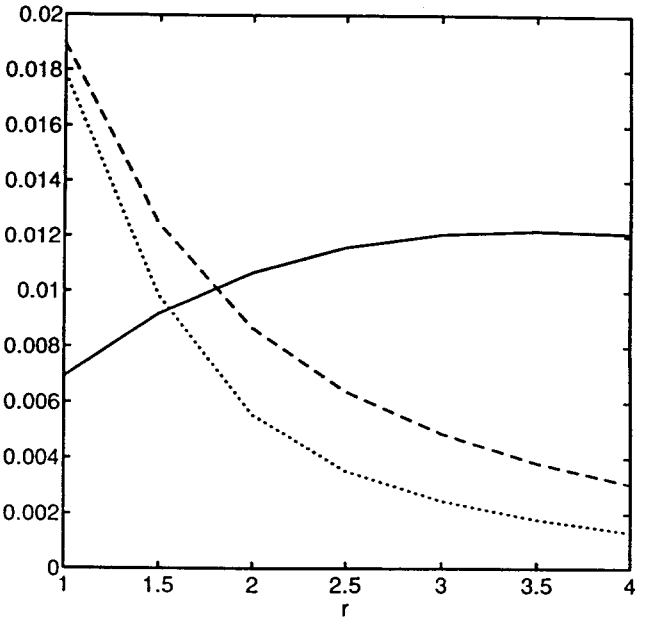

Fig. 18. Subgrid-term $\|A_{1,1}\|$ (solid) and discretization error $\|\beta_1\|$ as a function of $r = \Delta/h$ for the second- (dashed) and fourth-order (dotted) accurate discretization method; 32^3-grid.

the fundamental instability rolls up and produces four rollers of mainly negative spanwise vorticity. These rollers rotate around each other in such a way that two pairs are formed. Within each pair the rollers merge and as a result the layer contains two highly three-dimensional rollers at $t = 40$ with a reasonable amount of positive spanwise vorticity. Another pairing, accomplished at $t = 80$, yields a single roller in which the spanwise vorticity exhibits a complex structure with many positive regions. This structure is an effect of the transition to turbulence which has been triggered by the pairing at $t = 40$ [15]. In order to check the accuracy of the simulation an additional run is performed with a different numerical method, which is fourth-order accurate in space for the convective terms. When compared with the second-order simulation, the evolution of the vorticity thickness, which is a sensitive quantity, shows differences up to 10 per cent. The evolution of other quantities is much more accurate; for example the momentum thickness [33] is the same within half a per cent. Moreover, a repetition of this simulation using 192^3 cells showed that converged results are obtained on 128^3 cells. If we simulate with these two numerical methods on a coarse grid of 64^3 cells, much larger differences are observed. The four results for the momentum thickness are shown in Fig. 17. From these considerations we conclude that the accuracy of the 128^3-DNS is sufficient for our purposes. We also checked that the conclusions drawn in this section equally apply when the 64^3-DNS is used.

In the following we will focus on two aspects: the role of the discretization error in LES and the correlation of subgrid-models. We use the DNS-database at $t = 70$, which is just before the last pairing has been completed. The coarse LES-grid which we consider contains 32^3 cells ($h = L_1/32$). Figure 18 shows the subgrid-term $A_{1,1} = \partial_j(\bar{\rho}_{1j})$ and the discretization error β_1 defined in (22) for the second- and fourth-order accurate method as functions of the ratio $r = \Delta/h$. If we compare this with Fig. 7, corresponding to the 2D-case, we observe that $A_{1,1}$ only slowly increases and eventually decreases if r is increased. This different behaviour

Table 3. Correlation coefficients for several subgrid-models.

model	$\overline{\rho u_1}$-equation	$\overline{\rho u_2}$-equation	$\overline{\rho u_3}$-equation
Smagorinsky	0.35	0.25	0.38
Clark *et al.*	0.97	0.95	0.96
Bardina	0.92	0.89	0.91

is a consequence of the difference between the slope of the energy spectrum in 2D and 3D. This slope is approximately -4 in 2D, while it is roughly $-5/3$ in 3D as was calculated from the DNS results [20]. However, the conclusions on the discretization error drawn from the analysis in 3D are the same as in 2D. The magnitude of the discretization error is larger than the subgrid-term for both second- and fourth-order accurate methods. Discretization errors are smaller than subgrid-terms, if the ratio r is sufficiently large. Moreover in that regime fourth-order discretizations are more accurate than second-order discretizations. We have not only considered the momentum equation for $\overline{\rho u_1}$, but calculated the subgrid-terms and discretization errors in the equations for $\overline{\rho u_2}$ and $\overline{\rho u_3}$ as well. No significant differences with the results for the $\overline{\rho u_1}$-equation, discussed above, were found.

Next we use the results at $t = 70$ in order to determine the correlation of the turbulent stress with the turbulent stress prescribed by the three models introduced in subsection 4.3. Table 3 presents the correlations for $\Delta = L_1/32$. As in the 2D-case we observe that the two non-eddy viscosity models correlate much better than Smagorinsky's model, which is of the eddy-viscosity type. Similar values are obtained if we use a database which corresponds to a different time (e.g. $t = 80$).

6. Conclusions

We have performed a priori tests of LES, in which we focussed on a classification of the (subgrid)-terms, the role of the discretization error and the correlation of some subgrid-models. For this purpose we filtered the results of reliable direct numerical simulations of the compressible mixing layer in two and three dimensions. The magnitudes of the (subgrid)-terms which occur in the filtered equations for compressible flow have been calculated and, as a consequence, they could be classified quite naturally in four groups. The classification shows that subgrid-models which incorporate the energy equation should at least take into account the divergence pressure velocity term B_1, pressure dilatation term B_2 and the divergence turbulent stress velocity term B_3. A model for B_3 is obvious, if a model for the turbulent stress is available. For the subgrid-term B_1 an eddy-diffusivity hypothesis is usually adopted. The subgrid-term B_2 however, is often neglected in subgrid-models for the energy equation, which is inconsistent. These a priori results were shown in detail for the 2D temporal application which shows the evolution of predominantly large scale structures and only a small amount of small scale influences as was inferred from the high value of the slope in the tail of the energy spectrum. In the 3D simulation a well developed turbulent flow field resulted. However, the main conclusions on the subgrid terms appear to be quite comparable to the 2D results, in spite of the significant differences between the 2D and 3D simulations. For example the correlation of the subgrid models with the turbulent stress was found to be low for eddy viscosity models

and high for the Clark and Bardina models, roughly independent of the dimension, i.e. of the amount of small scale structures.

Moreover we have shown that discretization errors are larger than subgrid-terms if the filter width Δ equals the grid size h, although most modern LES research is based on the proposition $\Delta = h$. This was observed for both a second-order and a fourth-order accurate discretization method. Consequently, the accuracy of LES is not adequate in this regime and quantitative predictions may be questionable. Furthermore, we have presented numerical evidence to support the hypothesis that simulations with Δ sufficiently larger than h result in smaller numerical errors. This increased accuracy is more significant if higher than second-order accurate discretizations are used. Another aspect of LES which we have analysed is the performance of three subgrid-models. It turns out that the non-eddy-viscosity models investigated correlate considerably better with the exact turbulent stress than Smagorinsky's model, which is of the eddy-viscosity type.

This study has been restricted to a priori tests of LES. We hope that a future study, which will incorporate a posteriori tests of LES, will yield further insight into the issues discussed above.

Acknowledgement

The calculation time for the 3D simulations was provided by the Stichting Nationale Computerfaciliteiten (National Computing Facilities Foundation, NCF), which is financially supported by the Nederlandse Organisatie van Wetenschappelijk Onderzoek (Netherlands Organization for Scientific Research, NWO).

References

1. J. Smagorinsky, General circulation experiments with the primitive equations. *Mon. Weather Rev.* 91 (1963) 99–164.
2. R.S. Rogallo and P. Moin, Numerical simulation of turbulent flows. *Ann. Rev. Fluid Mech.* 16 (1984) 99–137.
3. R.A. Clark, J.H. Ferziger and W.C. Reynolds, Evaluation of subgrid-scale models using an accurately simulated turbulent flow. *J. Fluid Mech.* 91 (1979) 1–16.
4. M.D. Love, Subgrid modelling studies with Burgers' equation. it J. Fluid Mech., 100 (1980) 87–100.
5. U. Piomelli, W.H. Cabot, P. Moin and S. Lee, Subgrid-scale backscatter in transitional and turbulent flows. In *Proceedings of the Summer Program 1990.* Center for Turbulence Research, Stanford (1990), 19–30.
6. U. Piomelli, T.A. Zang, C.G. Speziale and M.Y. Hussaini (1990). On the large-eddy simulation of transitional wall-bounded flows. *Phys. Fluids A* 2, 257–265.
7. W.C. Reynolds, The potential and limitations of direct and large eddy simulations. In J.L. Lumley, ed., *Whither Turbulence? Turbulence at Crossroads*, pp. 313–341. Springer-Verlag, Berlin.
8. T.A. Zang, R.B. Dahlburg and J.P. Dahlburg, Direct and large-eddy simulations of three-dimensional compressible Navier-Stokes turbulence. *Phys. Fluids A* 4, (1992) 127–140.
9. A.W. Vreman, B.J. Geurts, J.G.M. Kuerten, First ERCOFTAC *Workshop on Direct and Large Eddy simulation*, 28–30 March, Guildford, England, To appear, (1994).
10. B.J. Geurts, B. Vreman, H. Kuerten, V. Theofilis, *Proceedings 2nd International Symposium on Engineering Turbulence Modelling and Measurements*, Florence 31 May–2 June 1993; Ed: W. Rodi, F. Martelli, Elsevier (1993) 325.
11. B. Vreman, B.J. Geurts, H. Kuerten, Realizability conditions for the turbulent stress tensor in Large Eddy Simulation, *J. Fluid Mech.* To appear, (1994).
12. M. Lesieur, C. Staquet, P. Le Roy and P. Comte, The mixing layer and its coherence examined from the point of view of two-dimensional turbulence, *J. Fluid Mech.* 192 (1988) 511–534.
13. P.G. Saffman, Stud. Appl. Math., 50 (1971) 277.
14. G. Falkovich, A. Hananay, Is 2D turbulence a conformal turbulence?, *Phys. Rev. Lett.* 71 (1993) 3454.
15. R.D. Moser and M. Rogers. The three-dimensional evolution of a plane mixing layer: pairing and transition to turbulence. *J. Fluid Mech.* 247 (1993) 275–320.

16. P. Comte, M. Lesieur and E. Lamballais, Large and small-scale stirring of vorticity and a passive scalar in a 3D temporal mixing layer. *Phys. Fluids A*, 4, (1992) 2761–2778.
17. N.D. Sandham and W.C. Reynolds, Three-dimensional simulations of large eddies in the compressible mixing layer. *J. Fluid Mech.*, 224 (1991) 133–158.
18. F.J. Brandsma, *Mathematical and Physics Aspects of Simulations Based on the Navier-Stokes Equations.* ISNaS 88.08.024/NLR TP 89069 L (1989).
19. A. Favre, Turbulence: space-time statistical properties and behavior in supersonic flows. *Phys. of Fluids*, 26 (1983) 2851–2863.
20. M. Lesieur, *Turbulence in Fluids*, Kluwer Acad. Publ., Dordrecht (1990).
21. S.A. Ragab and J.L. Wu, Linear instabilities in two-dimensional compressible mixing layers. *Phys. Fluids A*, 1, (1989) 957–966.
22. W. Blumen, Shear layer instability of an inviscid compressible fluid. *J. Fluid Mech.*, 40, (1970) 769.
23. J.G.M. Kuerten, B.J. Geurts, J. van der Burg, A.W. Vreman, P.J. Zandbergen, Proceedings 13th International conference on numerical methods in fluid dynamics, Eds: M. Napolitano, F. Sabetta, Springer, 529, (1993).
24. A.W. Vreman, B.J. Geurts, J.G.M. Kuerten and P.J. Zandbergen, (1992). A finite volume approach to large eddy simulation of compressible, homogeneous, isotropic, decaying turbulence, *Int. J. Num. Meth. Fluids*, 15, 799–816.
25. V. Theofilis, A.W. Vreman, B.J. Geurts and J.G.M. Kuerten, 'A finite volume study of compressible shear layer instabilities' ASME FED-Vol. 155, 71, (1993).
26. B. Vreman, B.J. Geurts, H. Kuerten, Comm. Num. Meth. Eng. Math., To appear (1994).
27. U. Schumann, *Direct and large eddy simulation of turbulence – summary of the state-of-the-art 1991*. Lecture Series 1991-02: Introduction to the modelling of turbulence, Von Karman Institute, Brussels (1991).
28. M. Germano, Differential filters for the large eddy numerical simulation of turbulent flows. *Phys. Fluids* 29, (1986) 1755–1757.
29. J. Bardina, J.H. Ferziger and W.C. Reynolds, *Improved turbulence models based on LES of homogeneous incompressible turbulent flows.* Department of Mechanical Engineering, Report No. TF-19, Stanford.
30. K. Akselvoll and P. Moin, Large eddy simulation of a Backward Facing Step Flow. In W. Rodi and F. Martelli, eds., *Engineering Turbulence Modelling and Experiments 2*. Elsevier, Amsterdam (1993) 303–313.
31. M. Bohnert and J.H. Ferziger, The dynamic subgrid scale model in large-eddy simulation of the stratified Ekman layer. In W. Rodi and F. Martelli, eds. Elsevier, Amsterdam (1993) 315–324.
32. K. Horiuti, The role of the Bardina model in LES of turbulent channel flow. *Phys. Fluids A* 1 (1989) 426–428.
33. C.E. Leith, Stochastic backscatter in a subgrid-scale model: Plane shear mixing layer. *Phys. Fluids A* 2, (1990) 297–299.